Steady-state and time resolved laser spectroscopy of Cr^{3+} in lead-based fluoride glasses

1991 J. Phys.: Condens. Matter 3 7695

(http://iopscience.iop.org/0953-8984/3/39/015)

J. Phys.: Condens. Matter 3 (1991) 7695–7708. Printed in the UK

Steady-state and time resolved laser spectroscopy of Cr^{3+} in lead-based fluoride glasses

R Balda†, J Fernández†, M J Elejalde†, M A Illarramendi† and C Jacoboni‡

† Departamento de Física Aplicada I, Escuela Técnica Superior de Ingenieros Industriales y de Telecomunicación, Universidad del País Vasco, Alameda Urquijo s/n 48013 Bilbao, Spain

‡ Laboratoire des Fluorures, UA CNRS 449, Faculté des Sciences, Université du Maine, 72017 Le Mans Cédex, France

Received 16 April 1991, in final form 17 June 1991

Abstract. The optical properties of Cr^{3+} ions in lead-based fluoride glasses (PBI, PZG) have been investigated. Optical absorption, emission, lifetimes, and time resolved spectra were measured. The thermal quenching of the broadband emission is discussed in terms of the quantum mechanical single configurational coordinate (QMSCC) model using the Struck and Fonger method, and a good agreement with the experimental results is obtained. In order to correlate glass matrix composition with emission spectral properties, detailed time-resolved measurements have been performed. The obtained results provide a first insight into a possible site distribution of Cr^{3+} in these glasses.

1. Introduction

In the last few years there has been increasing interest in the optical spectroscopy of Cr^{3+} ions in glasses [1–13]. For low-field site ions the lowest excited $^4T_2$ level couples strongly to local and bulk vibrations giving a large homogeneous broadening for the $^4T_2 \rightarrow {}^4A_2$ transitions. In addition, in glass hosts there are a large variety of Cr^{3+} sites with different crystal-field strengths, and as a consequence there is an additional large inhomogeneous broadening [14]. It is these $^4T_2 \leftrightarrow {}^4A_2$ broad absorption and emission bands which are of interest for applications in lasers [15], and solar concentrators [16]. However, there have been only a few studies on the optical properties of chromium (III) in fluoride glasses, because of the low efficiency and thermal quenching of the emission [4]. More recently, the low quantum efficiency of chromium doped glasses has been explained in terms of the loose nature of the glass structure and the importance of local bonding requirements in determining the environment of the Cr^{3+} ions in the glass [10, 17, 18].

The aim of this work is to characterize the optical properties of Cr^{3+} in lead-based fluoride glasses (PBI and PZG) and to study the influence of the glass composition on its spectral and temperature behaviour. It will be shown that the quantum mechanical single configurational coordinate (QMSCC) model [19] (no linear coupling) gives a qualitative prediction of the temperature dependence of the non-radiative probabilities of the $^4T_2 \rightarrow {}^4A_2$ emission for these samples.

0953-8984/91/397695 + 14 $03.50

In order to give a more detailed insight into the nature of the emitting Cr^{3+} sites, time-resolved photoluminescence measurements have been performed for both glasses.

2. Experimental techniques

The fluoride glasses used in this study were prepared at the University of Maine, Le Mans, France. Samples were obtained by adding 0.5 wt.% CrF_3 to mixtures with the composition in mol%:

$$20PbF_2–25BaF_2–50InF_3–5ZnF_2–5YF_3–2AlF_3 \text{ (PBI)}$$

$$36PbF_2–24ZnF_2–35GaF_3–5YF_3–2AlF_3 \text{ (PZG)}$$

PZG and PBI glasses [20] were prepared from mixtures of the fluorides which are heated and melted at 750 °C in a platinum crucible, then cast on a preheated brass mould. Because of the sensitivity of the fluorides to hydrolysis, all the work was done inside a dry gloves box. The samples were cut and polished with OH^- free solvent.

The sample temperature was varied between 4.2 and 300 K with a continuous flow cryostat. Conventional absorption spectra were performed with a CARY 17 spectrophotometer. The emission measurements were made using the 633 nm emission line of a 15 mW HeNe laser and the 514 nm line of an argon laser as exciting light. The exciting light was chopped at 200 Hz. The fluorescence was analysed with a 0.22 m SPEX monochromator, and the signal was detected by a Hamamatsu R7102 extended infrared photomultiplier, and finally amplified by a standard lock-in technique. The system response was calibrated with a standard tungsten-halogen lamp which was also calibrated, against a National Bureau of Standards (NBS) lamp, in order to correct the emission spectra.

Lifetime measurements were performed with a tunable dye laser (1 ns pulse width), pumped by a pulsed nitrogen laser. In order to describe the evolution of fluorescence, time resolved spectroscopy has been used. The emission measurements were obtained by exciting the sample with a tunable dye laser and detecting the emission with a Hamamatsu R7102 photomultiplier. The spectra were processed by an EGG-PAR boxcar integrator.

3. Experimental results

3.1. Absorption and emission spectra

In spite of the expected sensitivity to variations in the local Cr^{3+} environments, the main features of the absorption spectra of chromium (III) are only slightly influenced by the nature of the glass hosts [21]. This prominent role played by the bonding in the Cr^{3+} site can be understood by assuming that, on the average, the chromium ions occupy sites which have nearly octahedral symmetry due to the strong ligand field stabilization energy of Cr^{3+} in a six-fold coordination. Therefore the absorption and emission spectra are usually interpreted by the Tanabe–Sugano diagram for d^3 systems with octahedral coordination, at least as far as the energy levels are concerned [1, 4, 22].

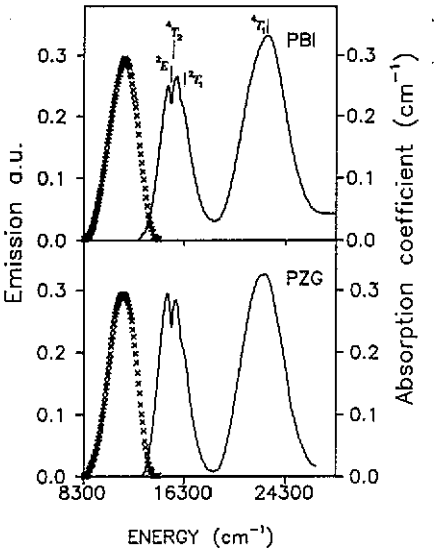

Figure 1. Absorption (full curve) and emission (×) spectra at LNT for PBI:Cr^{3+} and PZG:Cr^{3+} samples. The emission spectra were corrected for instrumental response and were obtained under excitation with the 633 nm line of a HeNe laser.

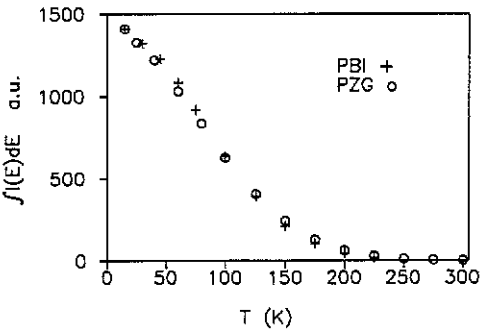

Figure 2. Integrated emission intensities $\int I(E)\,dE$ as a function of temperature for both samples. (+) PBI and (○) PZG.

Figure 1 shows the emission and absorption spectra of Cr^{3+} in PBI, and PZG obtained at liquid nitrogen temperature (LNT). The absorption spectra are characterized by two broad, spin-allowed, bands which can be identified as the vibronically broadened transitions $^4T_2 \leftarrow {}^4A_2$, $^4T_1 \leftarrow {}^4A_2$ in order of increasing energy. The low energy band shows a fine structure due to the spin-forbidden $^2E \leftarrow {}^4A_2$ and $^2T_1 \leftarrow {}^4A_2$ transitions. The assignment of this structure has been made following the Fano antiresonance interpretation [23, 24].

In agreement with the predictions of the d^3 Tanabe–Sugano diagram in octahedral symmetry, the energies of $^2E \leftarrow {}^4A_2$ ($\approx$15267 cm^{-1}) and $^2T_1$ ($\approx$16260 cm^{-1}) do not show any appreciable change with the host lattice, whereas the transition energies to $^4T_2$ and $^4T_1$ states do vary somewhat due to differences of the crystal field of the different hosts. The $^4T_1 \leftarrow {}^4A_2$ transitions are centred around 22811 cm^{-1} (PBI), and 22457 cm^{-1} (PZG), whereas the $^4T_2 \leftarrow {}^4A_2$ transitions occur around 15248 cm^{-1} (PBI), and 15267 cm^{-1} (PZG).

The emission measurements were made under excitation in the $^4T_2 \leftarrow {}^4A_2$ absorption band using the 633 nm line of a HeNe laser. Additional measurements under excitation in the $^4T_1 \leftarrow {}^4A_2$ absorption band will also be shown in section 4.3. The emission in these glasses is characterized by a broad and structureless band that corresponds to the $^4T_2 \rightarrow {}^4A_2$ transition. For a 633 nm excitation wavelength, as can be seen in figure 1 the peak position: 11414 cm^{-1} (PBI), and 11352 cm^{-1} (PZG), and the bandwidth: 1026 cm^{-1} (PBI), and 965 cm^{-1} (PZG), are similar for both samples. In all cases a large Stokes shift ($\approx$4000 cm^{-1}) is observed, indicating that a considerable change occurs in the ionic arrangement around Cr^{3+} in the excited state [17 and references therein]. In figure 2 a plot of the integrated emission intensity as a function of temperature for both samples is presented, and it shows that the intensity decreases as temperature increases which is due to increasing non-radiative processes.

Table 1. LNT spectroscopic data of both samples PBI: Cr^{3+} (0.5%), and PZG: Cr^{3+} (0.5%). Dq/B is the octahedral crystal field, f is the oscillator strength of the $^4T_2 \leftarrow {}^4A_2$ transition, $(Dq/B)_{RES}$ is the crystal field for the relaxed excited state, ΔE_S is the Stokes shift, τ_R is the radiative lifetime of the $^4T_2 \rightarrow {}^4A_2$ emission and τ_{exp} is the average lifetime monitored at the emission peak.

	Dq/B	f	$(Dq/B)_{RES}$	ΔE_s (cm^{-1})	τ_R (μs)	τ_{exp} (μs)
PBI	2	1.93×10^{-5}	1.47	4134	241	71
PZG	2.03	2.06×10^{-5}	1.5	3995	218	68

Table 1 contains a summary of LNT spectroscopic data of Cr^{3+} in these glasses. The crystal field parameters Dq and B were calculated by using the Tanabe–Sugano matrix elements [25]. The $^4T_2$ emission peak position was used to determine a value of Dq/B for the relaxed excited state (RES) from the formula

$$\left(\frac{Dq}{B}\right)_{RES} = \frac{E(^4T_2 \rightarrow {}^4A_2)}{10B} \qquad (1)$$

where E ($^4T_2 \rightarrow {}^4A_2$) is the energy of the peak position of the emission band, and the value of B is assumed to remain unchanged by the variation of the Cr–F distance.

The oscillator strengths, in absorption, have been estimated by using standard relations [26]. To estimate the radiative lifetime we use the approximate relation

$$f_{em}\tau_R = 1.51 \times 10^4 [9/n(n^2+2)^2]\,\lambda^2 \qquad (2)$$

where n is the refractive index ($n = 1.547$ for PBI, and $n = 1.578$ for PZG), λ is the emission peak in metre units, and f_{em} is the oscillator strength, which is related to the one in absorption f_{abs} by

$$f_{em}/f_{abs} = \omega_{em}/\omega_{abs} = \lambda_{abs}/\lambda_{em} \qquad (3)$$

where λ_{abs} and λ_{em} are the peak positions of absorption and emission of the $^4T_2 \leftrightarrow {}^4A_2$ transition respectively [13]. A more accurate relation can be found in the McCumber theory [27], but such refinement does not seem to be justified in this study.

3.2. Emission lifetime results

The decay kinetics of the broad infra-red emission of both samples were studied as a function of temperature, emission, and excitation wavelength.

The observed decays measured along the broad emission band, under pulsed laser excitation, at the $^4T_2 \leftarrow {}^4A_2$, and $^4T_1 \leftarrow {}^4A_2$ absorption bands, are non-exponential throughout the whole temperature range. Figure 3 shows one of the LNT experimental fluorescence decays of PZG: Cr^{3+} monitored at 910 nm under excitation at 655 nm. As can be seen in the same figure, this decay is best described by the sum of two decaying exponentials. The figure 4(*a*) shows, as an example, the logarithmic plot of the intensity decay (excited at 655 nm) at LNT for emission wavelengths at the blue and red sides of the emission band for the PZG sample. The short-lived and long-lived components of the experimental decays obtained by a least squares fit are around 30 μs, and 116 μs at LNT for an emission wavelength of 780 nm. It is evident, from the figure, that the time dependence of the decays varies across the broad emission band, shifting towards shorter

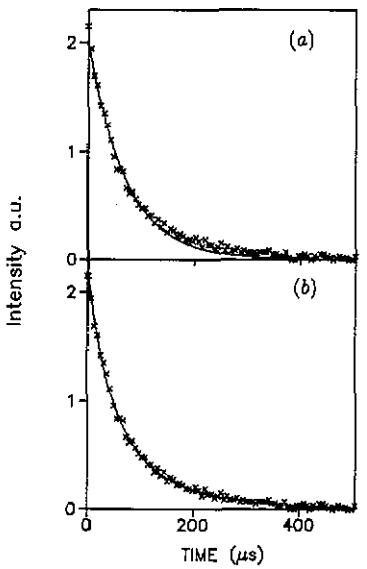

Figure 3. LNT experimental decay of the $^4T_2 \rightarrow {}^4A_2$ transition in PZG : Cr^{3+} glass, monitored at 910 nm for an excitation wavelength of 655 nm. (*a*) Fit to one exponential function (full curve), and experimental decay (×). (*b*) Fit to a double exponential function (full curve), and experimental decay (×).

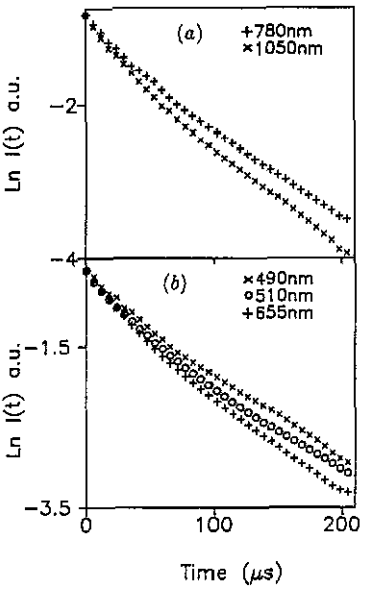

Figure 4. (*a*) Logarithmic plot of the decays of the $^4T_2 \rightarrow {}^4A_2$ transition in PZG : Cr^{3+} glass, monitored at 780 nm (+), and 1050 nm (×), for an excitation wavelength of 655 nm; (*b*) logarithmic plot of the decays monitored at 910 nm for different excitation wavelengths. (×) 490 nm, (○) 510 nm, and (+) 655 nm. Measurements were performed at 77 K.

decay times as the wavelength increases. In addition to the spectral dependence of the decays a dependence on the excitation wavelength is also observed. These data are plotted in figure 4(*b*). This graph shows the time decays of the luminescence monitored at 910 nm at three different excitation wavelengths. The excitations correspond to the energies of the peak position of the $^4T_2 \leftarrow {}^4A_2$ (655 nm), and the low energy side of the $^4T_1 \leftarrow {}^4A_2$ (490 nm, 510 nm) absorption bands respectively.

For practical purposes we shall use the 'average lifetime' defined by equation $\bar{\tau} = [\int tI(t)\,dt]/[\int I(t)\,dt]$ in the analysis which follows.

The spectral dependence of the decays along the broad emission band obtained at two different excitation wavelengths (510 nm, and 655 nm) are plotted in figure 5 for both samples. As can be seen in the PBI case, the lifetimes decrease as the wavelength increases throughout the emission band, and this behaviour is very similar for both excitation wavelengths. In the PZG case, lifetimes remain nearly constant on the high energy wing, and then decrease as the energy decreases, the wavelength slope being somewhat higher for the excitation at 510 nm.

Lifetime data, monitored at the peak position of the emission bands, and integrated emission intensities $\int I(t)\,dt$ as a function of temperature are shown in figure 6. The top graph shows the lifetimes and integrated intensities as a function of temperature for the PBI sample by exciting at 655 nm. The bottom graph presents lifetimes and integrated intensities for the PZG sample by exciting at 510 nm, and 655 nm. It is apparent from this figure that the emission lifetimes and the integrated intensities display a similar qualitative behaviour with temperature.

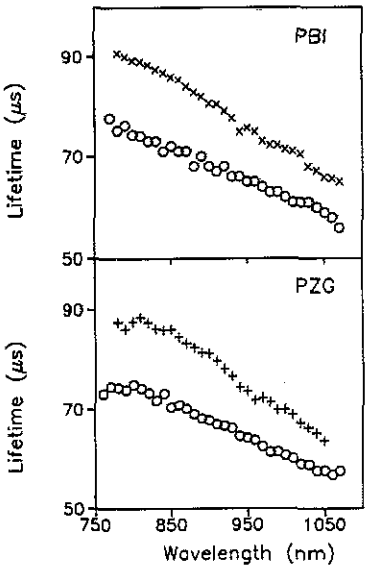

Figure 5. LNT lifetimes at different emission wavelengths along the $^4T_2 \rightarrow {}^4A_2$ emission band for two excitation wavelengths, 655 nm (○), and 510 nm (×, +). The data correspond to the average lifetime.

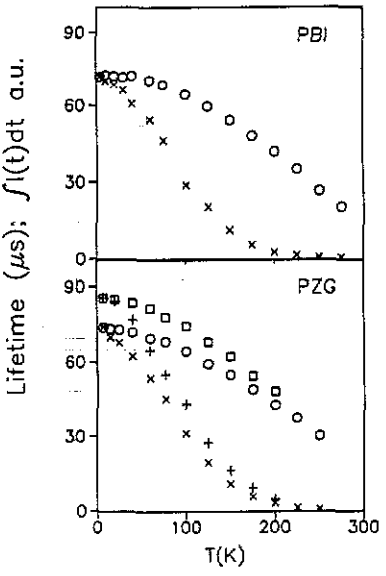

Figure 6. *Emission lifetimes and integrated* emission intensities as a function of temperature for Cr^{3+} in PZG and PBI. Lifetimes, and integrated intensities were obtained by exciting at 510 nm (□, +), and at 655 nm (○, ×) for PZG and at 655 nm (○, ×) for the PBI sample.

3.3. Time resolved spectra

The variation of fluorescence lifetime with emission wavelength, and the non-exponential character of the decays suggested the existence of some kind of site distribution for the Cr^{3+} ions. In order to obtain a more precise knowledge about this possibility, time resolved emission spectra were performed.

Time resolved emission spectra (TRS) were obtained at 77 K after exciting the samples with a tunable laser at the peak position of the $^4T_2 \leftarrow {}^4A_2$ absorption band (655 nm), and at the low energy side of the $^4T_1 \leftarrow {}^4A_2$ absorption band (510 nm). The evolution of the emission intensity at different time delays between 1 μs and 200 μs was investigated for both samples. At shorter time delays the spectra present similar features to the steady-state (SS) emission spectra, but for increasing time delays, they show a blue shift and a narrowing of the bandwidth. Figure 7 displays the first and second moments, calculated from the time resolved emission spectra, for PZG : Cr^{3+} as a function of time for two different excitation wavelengths. As shown in figure 7 the narrowing of the spectra and the peak shift obtained under excitation at 655 nm do not exhibit a monotonic variation when time increases, as was observed in other systems [28]. In this case the change of the second moment is more pronounced at the first 20 μs. This time roughly corresponds to the short-lived components of the decays. On the contrary, the narrowing of the spectra obtained by exciting at 510 nm exhibits a monotonic variation.

4. Discussion

4.1. Analysis of the emission spectra

The preceding spectroscopic data show that when Cr^{3+} is raised to the $^4T_2$ excited state, a large configurational relaxation occurs (RES) due to strong electron–phonon

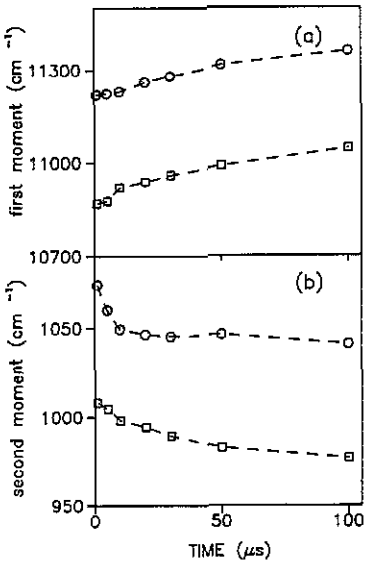

Figure 7. Time dependence of first and second moments obtained from the corrected time resolved emission spectra for PZG : Cr^{3+}. The time resolved emission spectra were obtained by exciting at 510 nm (□), and 655 nm (○) with time delays between 1 μs and 200 μs, and gate widths between 50 ns, and 1 μs. The spectra were performed at 77 K. The broken curves are only a guide for the eyes.

interactions. The spectroscopic features of the broad band emission from the RES level can usually be described by a single configurational coordinate (SCC) model. The parameters of this model, in the linear coupling approximation, were calculated from the moment analysis of the emission bands. The quantitative analysis of luminescence spectra required a transformation from corrected intensities to line shapes $G(E)$ [29]. The temperature dependence (4.2 K–300 K) of the second moment of the emission bands [30] allows us to estimate the average 'effective' frequency of the breathing mode and the average Huang–Rhys factor for both samples. The obtained values were $\hbar\omega_0 = 493\ cm^{-1}$ (PBI), $\hbar\omega_0 = 524\ cm^{-1}$ (PZG), and $S = 4.2$ (PBI), and $S = 2.9$ (PZG). From the relation $h\nu_{0cm} = U_0 - S\hbar\omega_0$, the value for the electronic energy gap U_0 at 4.2 K for each sample was also obtained. The activation energy corresponding to the crossover point of the ground and excited state potential energies was calculated by using the relation

$$E_A = (U_0 - S\hbar\omega_0)^2/4S\hbar\omega_0. \tag{4}$$

Taking the above mentioned S, $\hbar\omega_0$, and U_0 values, we found $E_A = 15393\ cm^{-1}$ (PBI), and $20429\ cm^{-1}$ (PZG).

The fit of the experimental emission line shape $G(E)$ to the theoretical one predicted by the SCC model with linear coupling (equation 2 in [31]), using the obtained model parameters, is shown for the PZG sample in figure 8. As can be seen it is quite poor, and the calculated Stokes-shift underestimates the experimental values. As we will show, this behaviour is consistent with the existence of some kind of site distribution for the Cr^{3+} ions in the glass matrices.

4.2. Thermal quenching

The strong temperature dependence of the emission shown in figure 2 indicates that both samples present a similar quenching mechanism. In a recent work [13] the authors have found an analogous temperature behaviour in other chromium doped fluoride

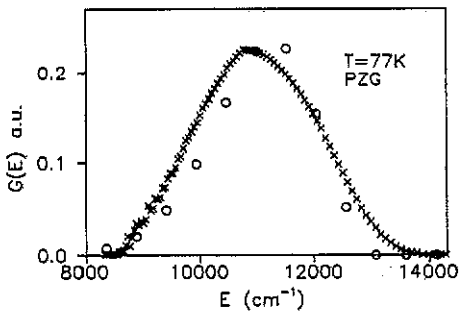

Figure 8. Fit of the experimental emission lineshape with the theoretical shape predicted by the SCC model with linear coupling at 77 K, using the values $S = 2.9$, and $\hbar\omega_0 = 524\ \text{cm}^{-1}$, obtained from the temperature dependence of the emission bandwidth. (×) Experimental. (○) Fit to equation (2) in [31].

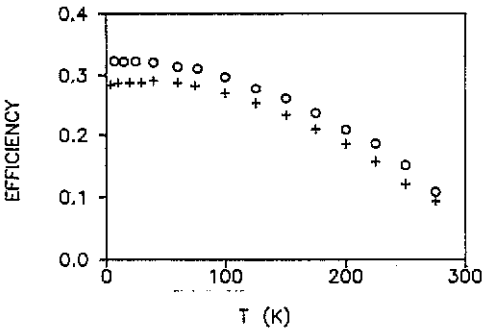

Figure 9. Quantum efficiency (QE) as a function of temperature for Cr^{3+} in the matrices PZG (○), and PBI (+).

glass. In this work [13] the strong thermal quenching of the emission was most likely attributed to the dominance of multiphonon emission processes.

Under this assumption the experimental transition rate can be written as

$$\tau_{\text{exp}}^{-1} = \tau_{\text{R}}^{-1} + W_{\text{NR}} \tag{5}$$

where τ_{exp} is the measured lifetime and τ_{R} represents the radiative lifetime, which is related to the electric dipole oscillator strength f_{em} by (2). From the measured values of the oscillator strengths at different temperatures we find a low increase of τ_{R}^{-1} with temperature, which is probably due to an enhancement of the vibronic processes. The τ_{R}^{-1} rates can be fitted along the temperature range of interest to the empirical formula [32]

$$\tau_{\text{R}}^{-1} = \tau_0^{-1} \exp(\alpha T) \tag{6}$$

and then, the temperature dependence of W_{NR} can be calculated from (5). As we shall see W_{NR} rapidly increases with temperature in both hosts above 77 K. The relative quantum efficiencies (QE) calculated by the expression $\eta = \tau_{\text{exp}}/\tau_{\text{R}}$ as a function of temperature are displayed in figure 9. As can be seen QE rapidly decreases as temperature increases above 150 K, which is a typical behaviour of Cr^{3+} in glasses [4]. These low QE values are in accordance with the loose structure of glassy systems. The large rearrangement of the ionic environment between $^4A_2$ and $^4T_2$ are consistent with the observed Stokes shift, which can be related to an increase of multiphonon emission rates [13, 14, 17, 18]. In our case, the largest Stokes shift found for the PBI compound corresponds to the lowest value for QE.

In the work mentioned above [13] the authors found the model proposed by Struck and Fonger [19] to be adequate for a qualitative understanding of the temperature quenching of the broadband luminescence of Cr^{3+} in BIGAZYT fluoride glass. According to these results, we tried to fit the observed temperature dependence using the current

Table 2. Parameters of the SCC model with different force constants ($\Theta = 42.3°$) for PZG : Cr^{3+}.

S_u	$\hbar\omega_u$ (cm^{-1})	S_v	$\hbar\omega_v$ (cm^{-1})	U_0 (cm^{-1})	E_A (cm^{-1})
3.14	586	2.6	485	13048	7539

SCC model with different force constants for the ground and excited states. In this model the non-radiative decay rate at temperature T can be written as

$$W_{NR}(T) = A_{uv}U_{p_u} \tag{7}$$

where A_{uv} is an electronic factor, and U_{p_u} is given by

$$U_{p_u} = \sum (1 - r_v)r_v^m U_{p_u,m}^2. \tag{8}$$

For parabolic energy potentials, $U_{p_u,m}^2$ are the 'Franck–Condon factors' (FC) given by the Manneback recursion formula [19] and $(1 - r_v)r_v^m$ are the initial v-state thermal weights, where r_v is the Boltzman factor $\exp(-\hbar\omega_v/KT)$ for the initial state phonon energy $\hbar\omega_v$. For the non-radiative transition, the initial m and final n energy levels match, and the number p_u of phonons generated in the transition is defined by the zero phonon transition energy divided by the average phonon energy for the u level $\hbar\omega_u$. The average m through which the non-radiative transition occurs is given by

$$\langle m \rangle_p = \sum m(1 - r_v)r_v^m U_{p_u,m}^2. \tag{9}$$

In this model the Manneback angle is defined by $\tan^2\Theta = \omega_v/\omega_u$ where ω_v and ω_u are the vibrational frequencies for the excited v and ground u states ($\Theta = 45°$ for linear coupling).

Table 2 shows the parameter values of the model [19, 33] for the PZG sample for a Mannebak angle $\Theta = 42.3°$. Figure 10 shows the measured temperature dependence of W_{NR}, and the predicted quenching from (7), for PZG : Cr^{3+}, taking the parameters from table 2 and an electronic factor $A_{uv} = 10^{13}\ s^{-1}$. After scaling W_{NR} values for comparison, a good qualitative agreement for the temperature dependence of W_{NR} can be seen.

Table 3 shows the breakdown of the non-radiative rates for the $^4T_2(v) \rightarrow {}^4A_2(u)$ non-radiative transitions. The mean vibrational level at which the non-radiative transition occurs is closer to the v parabola minimim than to the v, u crossover. The mean level is 1.972 at 300 K, whereas the crossover is at $m = 16$. Calculation details of the parameters in tables 2 and 3 can be found in [19] and [33].

Figure 11 shows, as an example, a configuration coordinate diagram for PZG : Cr^{3+}, using the parameters obtained for linear coupling, and for different force constants with $\Theta = 42.3°$. The solid lines correspond to the potential energy wells of the electronic ground (u), and excited (v) states for $\Theta = 42.3°$, whereas the symbols correspond to linear coupling. As we can see, the curve crossing energy E_A decreases by a third of its value when Θ decreases from 45° to 42.3° giving a lower value for the electronic coupling.

We made no effort to calculate absolute values of W_{NR}, as current theories do not seem adequate for this task. Nor did we attempt to analyse the data by using models of non-radiative decays which emphasize anharmonic effects.

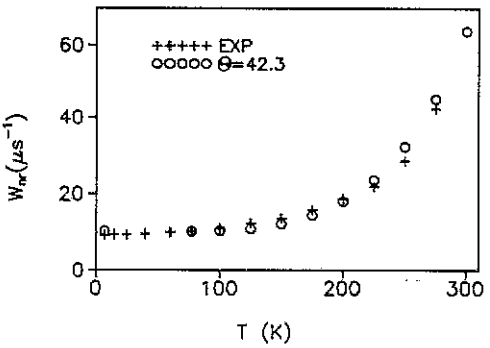

Figure 10. Temperature dependence of measured W_{NR} (×) and the predicted quenching (○) for a PZG:Cr^{3+} sample, assuming a different force constant in the ground and excited states for a Manneback angle Θ = 42.3°.

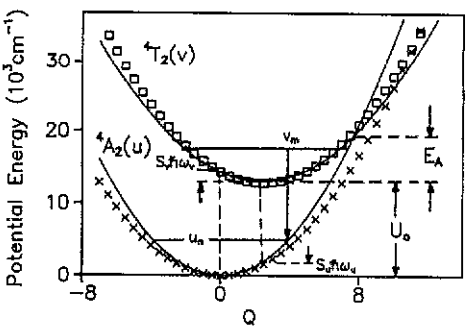

Figure 11. Single configuration coordinate diagram for PZG:Cr^{3+} based on the parameters obtained for linear coupling (Θ = 45°), and for a Manneback angle of 42.3°. Solid lines correspond to the potential energy wells of the electronic ground (u) and excited (v) states for Θ = 42.3°, and symbols correspond to linear coupling. U_0 represents the electronic gap, S is the Huang–Rhys factor, u_n and v_m are the initial and final vibrational wavefunctions, $S_u\hbar\omega_u$, and $S_v\hbar\omega_v$ are the relaxation energies after emission and absorption respectively, and E_A is the curve crossing energy. Linear coupling corresponds to $\hbar\omega_u = \hbar\omega_v = \hbar\omega_0$ and $S_u = S_v = S$.

Table 3. Calculations of W_{NR}, $\langle m\rangle_p$ at four temperatures for a Manneback angle Θ = 42.3° for PZG:Cr^{3+}.

		$A_{uv}(1-r_v)r_c^m U_{23+m,m}^2$			
m	$U_{23+m,m}^2$	0 K	77 K	150 K	300 K
0	8.267×10^{-10}	8.262×10^3	8.261×10^3	8.183×10^3	7.456×10^3
1	1.980×10^{-8}		2.281×10^1	1.865×10^3	1.743×10^4
2	2.052×10^{-7}		2.723×10^{-2}	1.838×10^2	1.761×10^4
3	1.364×10^{-6}		2.085×10^{-5}	1.162×10^1	1.142×10^4
4	6.713×10^{-6}		1.182×10^{-8}	5.440×10^{-1}	5.480×10^3
5	2.639×10^{-5}		5.353×10^{-12}	2.034×10^{-2}	2.101×10^3
6	3.280×10^{-5}		7.665×10^{-16}	2.404×10^{-4}	2.546×10^2
7	1.122×10^{-4}		3.020×10^{-19}	7.822×10^{-6}	8.495×10^2
8	7.692×10^{-4}		2.385×10^{-22}	5.100×10^{-7}	5.679×10^1
9	1.795×10^{-3}		6.412×10^{-26}	1.132×10^{-8}	1.293×10^1
10	3.731×10^{-3}		1.535×10^{-29}	2.237×10^{-10}	2.620
	$W_{NR} = A_{uv}U_p$	8.262×10^3	8.284×10^3	1.024×10^4	6.191×10^4
	$\langle m\rangle_{23}$	0	0.003	0.222	1.972
	Crossover energy	$m \approx 16$			

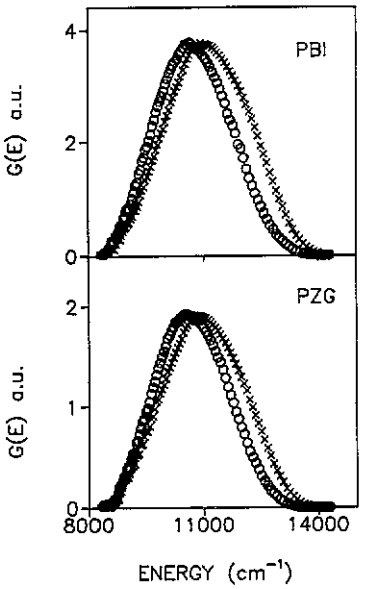

Figure 12. LNT steady-state (ss) emission spectra obtained by exciting at the $^4T_1 \leftarrow {}^4A_1$ absorption band with the 514 nm (○) line of an argon laser, and by exciting at the $^4T_2 \leftarrow {}^4A_2$ absorption band with the 633 nm (×) line of a HeNe laser. The corrected spectra have been normalized to have the same peak intensity.

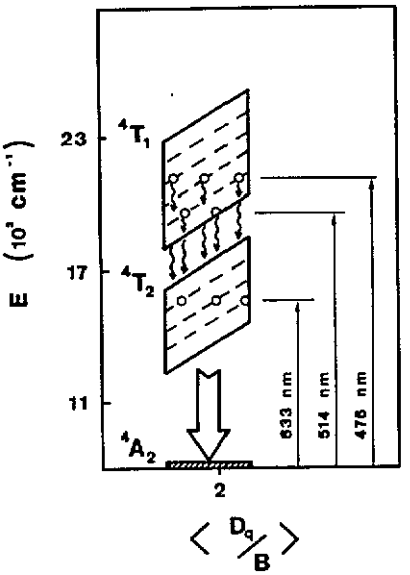

Figure 13. Extended Tanabe–Sugano diagram in fluoride glasses. The straight lines represent excitations, the broad arrows, emissions to the ground state, and the undulating lines, non-radiative relaxations.

4.3. Site dependent effects on fluorescence

As we mentioned before (section 3), Cr^{3+} ions occupy sites of nearly octahedral symmetry in glasses. The spread of Dq/B values from site-to-site gives a broad range of available energy levels, and allows the study of narrowing effects on the broad $^4T_2 \rightarrow {}^4A_2$ emission band as a function of laser excitation wavelength. Figure 12 shows the LNT steady-state (ss) fluorescence spectra of both samples following excitations into the $^4T_1$ and $^4T_2$ absorption bands. A narrowing ($\approx 55\ cm^{-1}$), and a red shift ($\approx 413\ cm^{-1}$) of the spectra can be observed as the excitation is changed from 633 nm to 514 nm for the PBI sample. A similar narrowing ($\approx 69\ cm^{-1}$), and red shift ($\approx 359\ cm^{-1}$) are also observed for the PZG sample (bottom of figure 12). These results can be qualitatively understood by the extended Tanabe–Sugano diagram shown in figure 13, which takes into account the spread of Dq/B values from different Cr^{3+} sites. When pumping with a 514 nm line on the long wavelength edge of the $^4T_1$ band, we selectively excite a lower number of sites with smaller Dq values. After a rapid non-radiative de-excitation to the lower $^4T_2$ level, these sites will give the observed narrowed fluorescence. If the pumping is performed with the 633 nm line at the high energy wing of the $^4T_2$ band, a larger amount of sites can be raised to the $^4T_2$ state giving, after relaxation to the lower $^4T_2$ levels, the broader observed emission spectra.

The existence of this broad site distribution is reflected by the wavelength dependence shown by lifetimes measured along the $^4T_2 \rightarrow {}^4A_2$ emission band. Figure 5 presents the

spectral dependence of average lifetimes for both compounds after excitation with 510 nm, and 655 nm laser lines. It is worthwhile noticing the monotonic decrease of lifetimes with increasing emission wavelength exhibited by PBI glass for both excitations. This behaviour should be expected because ions having large Dq values will have lower non-radiative transition probabilities and therefore, longer lifetimes. However, though shorter lifetimes should be expected for the high energy exciting wavelength (510 nm), the opposite occurs. A possible explanation for this result may be connected with the difference in the effective oscillator strength for the electronic transitions of low field (510 nm excitation line), and high field (655 nm excitation line) sites. Actually, lifetimes monitored at 900 nm obtained under excitation along the low energy side of the $^4T_1$ absorption band increase from 70 to 80 μs as the excitation wavelength changes from 485 to 515 nm.

The wavelength dependence of the average lifetimes of the PZG sample (figure 5) presents a different behaviour at the high energy wing of the emission band. The two steps suggested by the behaviour of lifetimes in this region would be difficult to understand if only one kind of site distribution were present because, as we mentioned before, in that case a monotonic behaviour should be expected [28]. It is interesting to notice that this effect is more pronounced under excitation with the 655 nm line, which suggests the existence of two subsets of Cr^{3+} centres with slightly different spectral dependences in the PZG matrix. In addition to this two-step behaviour of the average lifetimes, the biexponential character shown by the shape of the lifetime curves (see figure 3) under laser excitation also reinforces this hypothesis.

Time resolved emission spectroscopy may help to clarify our understanding of the Cr^{3+} site distributions. Figure 7 shows that the blue shift and narrowing of the luminescence undergo an abrupt change in the interval between 1 and 20 μs under excitation with the 655 nm line. This interval of time roughly covers the short-lived component of the experimental decays. This behaviour is consistent with the existence of two main site distributions with different time constants. On the contrary, under excitation with the 510 nm line only a low field subset of Cr^{3+} ions is excited giving the observed monotonic behaviour.

The site selectivity in time domain can be qualitatively observed by comparing SS and long time delayed emission spectra. On the top of figure 14 we can see the differences between both spectra scaled at the high energy wing of the emission band under excitation in the $^4T_2 \leftarrow {}^4A_2$ band. As can be observed this difference is nearly Gaussian and red shifted corresponding to the luminescence loss attributed to the low energy sites distribution. In the bottom of figure 14 the same difference is plotted for excitation in the $^4T_1 \leftarrow {}^4A_2$ band. It is apparent that in this case the difference between SS and time delayed fluorescence is less than in the former case in accordance with a reduced distribution of Cr^{3+} sites.

Previous structural studies by F^{19} NMR [34], EXAFS [35], neutron diffraction in the magnetic spin glass state [36, 37] and by Raman spectrometry [38] have led to a coherent view of the structure of transition metal fluoride glasses such as PZG, both in terms of polyhedra or in terms of packing of fluoride ions. From the first point of view, the corner sharing of $M^{III}F_6$, $M^{II}F_6$ octahedra form bidimensional ramified chains which are linked together to build a lacunar pseudo-tridimensional ReO_3 type network; $M^{III}F_6$ octahedra are more regular than $M^{II}F_6$ octahedra, which seems to ensure the connection of the chains; Pb^{2+} ions are located in large holes between the chains. In terms of packing of fluoride ions, numerous octahedral sites are available for M^{2+} and M^{3+} ions, and Pb^{2+} ions (same size as F^-) are distributed among the packing of F^-. The vitreous state could result from a disorder of Pb^{2+} ions location in the F^- packing.

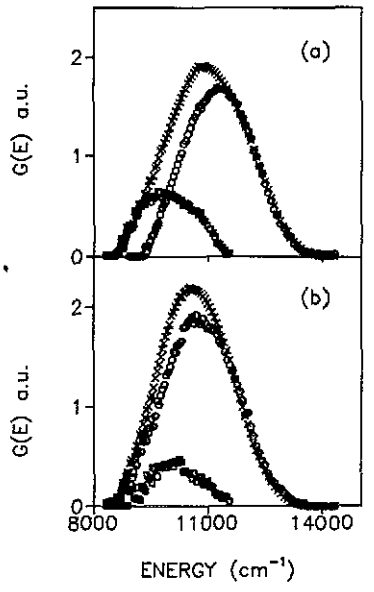

Figure 14. Comparison between scaled time resolved emission spectrum of the $^4T_2 \rightarrow {}^4A_2$ transition in PZG : Cr^{3+} at a time delay of 200 μs (○), and steady-state (SS) emission spectrum (×). The difference between both spectra is represented by (□). (*a*) The SS spectra was obtained by exciting at 633 nm, and the TRS spectra at 655 nm; (*b*) the SS and TRS spectra were obtained by exciting at 514 nm, and 510 nm respectively. Measurements were performed at 77 K.

The two different site distributions found for Cr^{3+} ions in PZG glass could correspond to the occupation of the two kinds of sites for octahedrally coordinated metals, most of them belonging to the regular $M^{III}F_6$ octahedron type (along the chains), and the rest to the distorted $M^{II}F_6$ octahedral type (with large M–F distances distribution) at the crossing of the chains.

5. Conclusions

From the discussion presented above, the following conclusions can be reached.

(i) The Cr^{3+} ions in lead-based fluoride glasses have a weak crystal field.

(ii) The QMSCC model with different constant forces gives a good qualitative agreement with the experimental temperature dependence of W_{NR} for these glasses.

(iii) Quantum efficiencies at room temperature are low in accordance with the strong thermal quenching of luminescence.

(iv) The spectral and time dependent properties of Cr^{3+} luminescence point out the assumption of the two main site distributions for Cr^{3+} ions in PZG glass.

Acknowledgments

This work was supported by the Comisión Interministerial de Ciencia y Tecnología (CICYT) of the Spanish Government (Ref 0188/89), Ministerio de Educación y Ciencia (Acción Integrada Hispano-Francesa 9A), and Basque Country Government (Ref 0008/89).

References

[1] Karapetyan G O, Lunter S G and Yudin D M 1963 *Opt. Spectrosc.* **14** 370
[2] Sharp E J, Miller J E and Weber M J 1973 *Appl. Phys.* **44** 4098
[3] Brawer S A and White W B 1977 *J. Chem. Phys.* **67** 2043
[4] Andrews L J, Lempicki A and McCollum B C 1981 *J. Chem. Phys.* **74** 5526
[5] Kisilev A and Reisfeld R 1984 *Solar Energy* **33** 163
[6] Van Die A, Blasse G and Van der Weg W F 1985 *J. Phys. C: Solid State Phys.* **18** 3379
[7] Van Die A, Blasse G and Van der Weg W F 1986 *Mat. Chem. Phys.* **14** 513
[8] Bergin F J, Donegan J F, Glynn T J and Imbusch G F 1987 *J. Lumin.* **36** 231
[9] Van Die A, Leenaers A C H I, Blasse G and Van der Weg W F 1988 *J. Non-Cryst. Solids* **99** 32
[10] Imbusch G F, Glynn T J and Morgan G P 1990 *J. Lumin.* **45** 63
[11] Kosch J, Seelert W and Strauss E 1990 *J. Lumin.* **45** 105
[12] Balda R, Illarramendi M A, Fernández J and Lucas J 1990 *J. Lumin.* **45** 87
[13] Illarramendi M A, Fernández J, Balda R, Lucas J and Adam J L 1991 *J. Lumin.* **47** 207
[14] Imbusch G F 1989 *Mat. Sci.* **XV** 61
[15] Kenyon P T, Andrews L J, McCollum B C and Lempicki A 1982 *IEEE J. Quant. Electron.* **18** 1189
[16] Reisfeld R 1985 *Mat. Sci. and Eng.* **71** 375
[17] Payne S A, Chase L L and Krupke W F 1987 *J. Chem. Phys.* **86** 3455
[18] Blasse G 1988 *Prog. Solid State Chem.* **18** 79
[19] Struck C W and Fonger W H 1975 *J. Lumin.* **10** 1
[20] Auriault N, Guery J, Mercier A M, Jacoboni C and De Pape R 1985 *Mat. Res. Bull.* **20** 309
[21] Tischer R E 1968 *J. Chem. Phys.* **48** 4291
[22] Schlafer H L, Gausmann H and Witzke H 1967 *J. Chem. Phys.* **46** 1423
[23] Fano J 1961 *Phys. Rev.* **124** 1866
[24] Lempicki A, Andrews L J, Nettle S, McCollum B C and Salomon E I 1980 *Phys. Rev. Lett.* **44** 1234
[25] Sugano S, Tanabe Y and Kamimura H 1970 *Multiplets of Transition-Metal Ions in Crystals* (New York: Academic) p 81
[26] Di Bartolo B 1968 *Optical Interactions in Solids* (New York: Wiley) p 410
[27] McCumber D E 1964 *Phys. Rev.* **136** 4A A954
[28] Weber M J, Brawer S A and DeGroot A J 1981 *Phys. Rev.* B **23** 11
[29] Wojtowicz A J, Kazmierczak M, Lempicki A and Bartram R H 1989 *J. Opt. Soc. Am.* **B6** 1106
[30] Lax M 1952 *J. Chem. Phys.* **20** 1752
[31] Struck C W and Fonger W H 1979 *J. Lumin.* **18/19** 101
[32] Andrews L J, Lempicki A, McCollum B C, Giunta C J, Bartram R H and Dolan J F 1986 *Phys. Rev.* B **34** 2735
[33] Fonger W H and Struck C W 1974 *J. Chem. Phys.* **60** 1994
[34] Dupas C, Le Dang K, Renard J P, Veillet P, Miranday J P and Jacoboni C 1981 *J. Physique* **42** 1345
[35] Le Bail A, Jacoboni C and De Pape R 1983 *J. Solid State Chem.* **48** 168
[36] Le Bail A, Jacoboni C and De Pape R 1985 *J. Non-Cryst. Solids* **74** 205
[37] Le Bail A, Jacoboni C and De Pape R 1985 *J. Non-Cryst. Solids* **74** 213
[38] Boulard B, Jacoboni C and Rousseau M 1989 *J. Solid State Chem.* **80** 17